Analysis and Compensation of the ZVS based Nonlinear Transfer Characteristic of a Dual Active Bridge

1st Fabian Sommer
Elektrotechnisches Institut
Karlsruhe Institute of Technology
Karlsruhe, Germany
fabian.sommer@kit.edu

2nd Tobias Merz
Elektrotechnisches Institut
Karlsruhe Institute of Technology
Karlsruhe, Germany
tobias.merz@kit.edu

3rd Hongyi Sui
Elektrotechnisches Institut
Karlsruhe Institute of Technology
Karlsruhe, Germany
hongyisui@outlook.com

4th Rüdiger Schwendemann
Elektrotechnisches Institut
Karlsruhe Institute of Technology
Karlsruhe, Germany
ruediger.schwendemann@kit.edu

5th Marc Hiller
Elektrotechnisches Institut
Karlsruhe Institute of Technology
Karlsruhe, Germany
marc.hiller@kit.edu

Abstract—This paper investigates the impact of Zero Voltage Switching (ZVS) on the transfer characteristic of a Dual Active Bridge (DAB). Various system and operational parameter are analyzed to distinguish their effects on the transfer characteristic. Furthermore, a comprehensive explanation of the nonlinear behavior inherent in the system is given. Given that this nonlinear behavior has the potential to diminish stability and reduce controller performance, a novel Measurement Data-Driven Function-Based Linearization (MFBL) method to ensure linearity is proposed. This method uses measurement data to derive an inverse function, which can subsequently be employed as a feedforward mechanism to mitigate the effects of nonlinearity. Importantly, this method does not necessitate an in-depth understanding of the system. This proposed approach is validated on a 40 kW DAB prototype and thereby confirms the efficiency of this method.

Index Terms—DCDC-Converter, Dual Active Bridge, Linearization, Soft Switching

I. INTRODUCTION

The Dual Active Bridge (DAB), introduced in 1991 [1], offers several advantages, including galvanic isolation, a wide operating range, Zero Voltage Switching (ZVS) capabilities, and high efficiency at high switching frequencies. These advantages, combined with advancements in semiconductor technology, especially in wide band gap materials and Medium Frequency Transformers (MFT), have led to its adoption in various applications. These applications range from grid applications for Solid State Transformers (SST) [2] to the integration of loads, power sources, and storage elements in DC grids [3] and DC fast charging with vehicle-to-grid (V2G) capabilities [4]. One significant advantage of the DAB converter over other DC/DC Converter technologies, such as the LLC converter, is its wide operation range regarding DC link voltages. However, this advantage comes with increased requirements for the voltage and current controller of the DAB, primarily due to the nonlinear transfer characteristics observed under Single Phase Shift (SPS) modulation [6]- [8]. This nonlinearity is mainly caused by resonant ZVS commutation and the associated deadtime T_{dt} [6]. This paper aims to comprehensively analyze the impact of various system and operational parameters on this nonlinearity. Additionally, a Measurement Data-Driven Function-Based Linearization (MFBL) method will be proposed to mitigate the effects of the ZVS commutation process on the DAB's transfer characteristic. Unlike the method shown in [5], the MFBL has low computational effort and Look up Table (LuT) requirements because only function paramter are stored for each voltage set instead of each operation point. Such efforts have the potential to enhance controller performance, particularly when employing a feedforward controller, as demonstrated in [10].

II. DAB WITH SINGLE PHASE SHIFT MODULATION

Figure 1 illustrates the equivalent circuit diagram of the DAB, accompanied by typical waveforms for Single Phase Shift (SPS) modulation depicted in Fig. 2. The control function of the DAB under SPS modulation is represented by (1), primarily dependent on the control variable φ, which signifies the phase shift between the two AC voltages v_{AC1} and v_{AC2}. In ideal DAB behavior, the AC voltages exhibit perfect rectangular waveforms, and the deadtime T_{dt} of each half bridge does not affect the current waveform significantly. The resulting current i_{AC}, illustrated in Fig. 2, assumes a trapezoidal shape. Depending on whether it is operating in buck or boost mode, the current i_{AC} is different and therefore may vary at the switching events 1 and 2.

$$P = \frac{1}{1/f_{\text{sw}}} \int_0^{1/f_{\text{sw}}} v_{\text{AC1}}(t) i_{\text{AC}}(t) \mathrm{d}t$$
$$= \frac{n V_{\text{DC1}} V_{\text{DC2}}}{2\pi f_{\text{sw}} L_\sigma} \cdot \varphi \cdot \left(1 - \frac{|\varphi|}{\pi}\right) \quad (1)$$
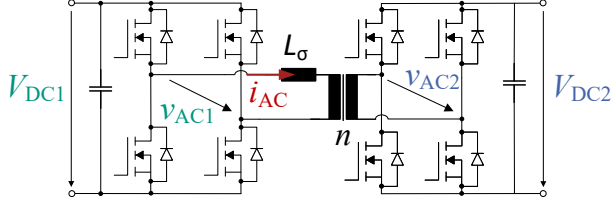

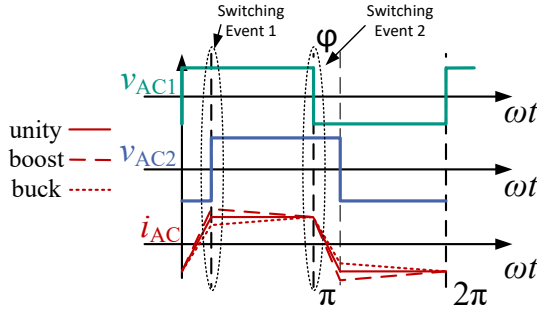Fig. 1. Equivalent circuit diagram of a DAB

Fig. 2. AC voltage v_{AC} and AC current i_{AC} waveforms for unity, buck and boost operation

III. IMPACT OF ZVS ON THE TRANSFER CHARACTERISTICS

The relationship between the phase shift angle φ and the transferred power P_{out} for SPS, as expressed in (1), is well-established and commonly employed. However, as the nominal power P_{out} of the DAB increases, the impact of nonlinear Zero Voltage Switching (ZVS) behavior becomes more pronounced. Higher power ratings necessitate larger chip areas and advanced SiC trench gate technologies, resulting in increased output capacitance of the semiconductor C_{OSS} and a required reduction of the transformer stray inductance L_σ to achieve higher maximum power [11]. Both effects contribute to slower resonant ZVS commutation and consequently, a higher necessary deadtime T_{dt}. This results in an increasing ratio of deadtime to switching period $\frac{T_{\text{dt}}}{T_{\text{period}}}$, thereby amplifying the impact of resonant ZVS commutation on the transfer characteristics of the DAB at higher power levels [6]. The AC voltage v_{AC} during the deadtime T_{dt} can be calculated according to (2), where C_{eq} represents the equivalent value of the nonlinear output capacitance C_{OSS} and mainly depends on three system parameters [6]:

- L_σ: AC circuit stray inductance

- C_{OSS}: semiconductor output capacitance
- T_{dt}: deadtime

as well as three operation point dependent parameter:

- I_{sw}: semiconductor current at start of the resonant commutation
- V_{sw}: semiconductor voltage at start of the resonant commutation (usually the DC link voltage)
- v_{ac2}: counter voltage at the other fullbridge

$$v_{\text{AC1}}(t) = -\sqrt{\frac{L_\sigma}{C_{\text{eq}}}} \cdot I_{\text{sw}} \cdot \sin\left(\frac{t}{\sqrt{L_\sigma C_{\text{eq}}}}\right) +$$
$$(V_{\text{sw}} - v_{\text{AC2}}) \left(\cos\left(\frac{t}{\sqrt{L_\sigma C_{\text{eq}}}}\right) - 1\right) + V_{\text{DC1}}$$
$$\text{for } 0 <= t < T_{\text{dt}} \quad (2)$$

Initially, the impact of operation point-dependent parameters is analyzed. By employing (2) and varying the input parameters, the resonant commutation waveforms depicted in Fig. 4 can be obtained. The voltage-time error Φ_{error}, which is the difference between ideal, instantaneous and real resonant commutation, can be computed according to (3) and is shown in the figures as the blue highlighted area.

$$\Phi_{\text{error}} = \int_0^{T_{\text{dt}}} v_{\text{AC,opt}}(t) - v_{\text{AC}}(t) dt \quad (3)$$

By comparing different switching currents I_{sw} in Fig. 4 (a) and 4 (b), a significant difference in voltage-time error Φ_{error} is evident. This scenario is common in SPS modulation for both buck and boost operations (cf. Fig. 2, switching event 2). The dashed current $i_{\text{AC,opt}}$ represents the theoretically optimal waveform for this operation point, while the solid line i_{AC} depicts the resulting current due to ZVS commutation. Additionally, the counter voltage v_{AC} also influences the voltage-time error Φ_{error}, as demonstrated by comparing the scenarios of switching event 1 and 2 in Fig. 4 (b) and (c). For a negative counter voltage (switching event 1), the voltage-time error is smaller. Since both cases occur in SPS operation, the voltage error does not necessarily cancel out. The resulting transfer characteristic caused by these commutation processes is shown in Fig. 5. The voltage time error Φ_{error} is depicted in Fig. ?? for buck, boost, and unity operations with SPS. The difference $\Phi_{\text{error,AC1}} - \Phi_{\text{error,AC2}}$ is directly proportional to the deviation of the actual transfer characteristic (TC) compared to the ideal one. It is possible to calculate an error φ_{error} using (4), which, when added to φ, yields φ_{actual} as per (5) for the control function of the DAB (1). Utilizing φ_{actual} results in the actual transfer characteristic, incorporating the ZVS-based voltage error $\Phi_{\text{error,AC1/2}}$.

$$\varphi_{\text{error}} = \frac{\Phi_{\text{error,AC1}} - \Phi_{\text{error,AC2}}}{(V_{\text{DC1}} + V_{\text{DC2}})} \cdot (2\pi \cdot f_{\text{sw}}) \quad (4)$$

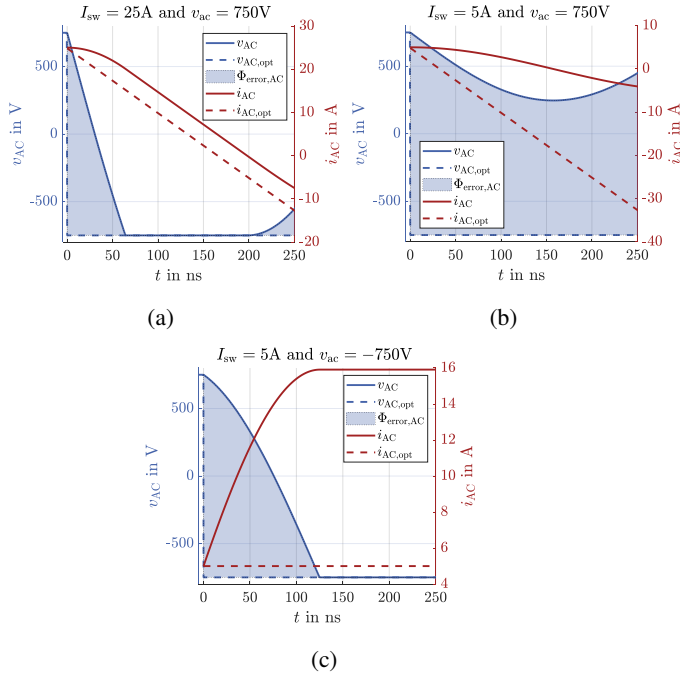$$\varphi_{\text{actual}} = \varphi + \varphi_{\text{error}} \quad (5)$$

Fig. 3. Calculated resonant commutation waveform (a) high current I_{sw} (b) low current I_{sw} with positive counter voltage v_{AC} (switching event 2) (c) low current I_{sw} with negative counter voltage v_{AC} (switching event 1)

Fig. 4. Calculated voltage time error Φ_{error} depending on the setpoint current I_{set} according to (3)

ZVS operation [6] and should therefore be avoided.

The resulting transfer characteristic due to the varying voltage-time error $\Phi_{\text{error,AC1/2}}$ is illustrated in Fig. 5 for buck, boost, and unity operations. Two distinct error characteristics can be identified depending on the voltage transfer ratio $\frac{V_{\text{DC1}}}{V_{\text{DC2}}}$ of the DAB. The first occurs around unity operation and is referred to as the small S-Shaped Function (cf. Fig. 5 blue), while the second is the big S-Shaped Function for high step-up or step-down operations (cf. Fig. 5 green and red). As the transfer ratio increases, the small S shape gradually transitions into the big S shape. Buck and boost operations exhibit a point symmetry with respect to the origin $(0,0)$.

The second group of parameters investigated in this chapter comprises the system parameters L_σ, $C_{\text{OSS}}/C_{\text{eq}}$, and T_{dt} and their impact on the transfer characteristics depicted in Fig. 5. An increase in stray inductance L_σ leads to a smaller range of the non-linear transfer characteristic for both the small and big S shapes (cf. Fig. 6 (a) and Fig. 7 (a)). This reduction is attributed to the expanded ZVS range of the DAB converter with higher stray inductances [6]. Additionally, the commutation process accelerates, thereby reducing the voltage-time error $\Phi_{\text{error,AC1/2}}$. Conversely, increasing the output capacitances of the MOSFETS C_{OSS} yields the opposite effect, as larger capacitances result in slower commutation and a diminished ZVS range (cf. Fig. 6 (b) and Fig. 7 (b)). Decreasing the deadtime T_{dt} has a similar impact to increasing the inductance L_σ, as it decreases the difference in voltage-time error $\Phi_{\text{error,AC1}} - \Phi_{\text{error,AC2}}$ (cf. Fig. 6 (c) and Fig. 7 (c)). However, it is worth noting that reducing the deadtime can lead to significantly increased losses due to incomplete
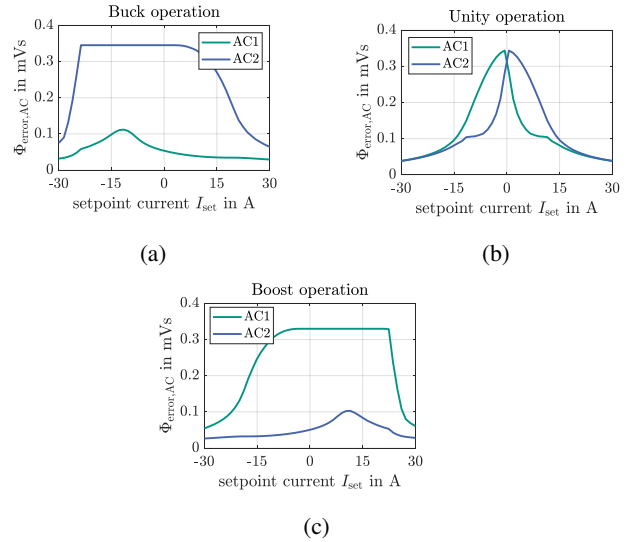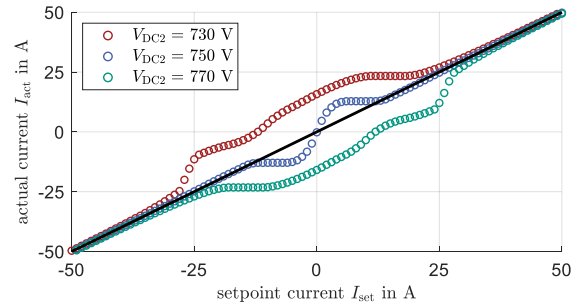

Fig. 5. Calculated resulting transfer characteristic of the DAB due to the ZVS transition for buck, boost and unity operation

IV. COMPENSATION METHOD

To address the SPS TC error discussed in section 3, a Measurement Data-Driven Function-Based Linearization (MFBL) method is employed. This technique utilizes measurement data to ascertain an invertible function $F_{\text{fit}}(I_{\text{set}})$. Subsequently, the inverted function $F_{\text{fit}}^{-1}(I_{\text{set}})$ is utilized in a feedforward compensation scheme to attain a linear transfer characteristic, expressed as $I_{\text{act}} = G_{\text{DAB}}(F_{\text{fit}}^{-1}(I_{\text{set}}))$ with G_{DAB} beeing the DAB transfer function. The block diagram of this method is depicted in Fig. 8. With this approach, system information is not required, and only measured transfer characteristics, encompassing all non-ideal effects of the DAB, are necessary. The algorithm for calculating the feedforward function F_{fit}^{-1} and its parameters is illustrated in Fig. 9. Three essential steps are involved:

- (Measurement) Data acquisition
- Curve fitting
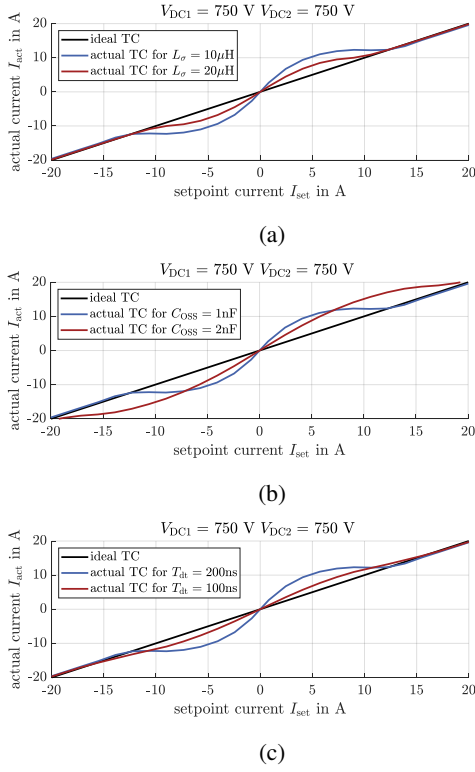- Evaluation and selection of best fitting function F_{fit}

Fig. 6. Variation of system parameter and influence on the calculated transfer characteristic in unity operation (a) L_σ (b) C_{OSS} (c) T_{dt} (All parameter according to table I if not stated otherwise)
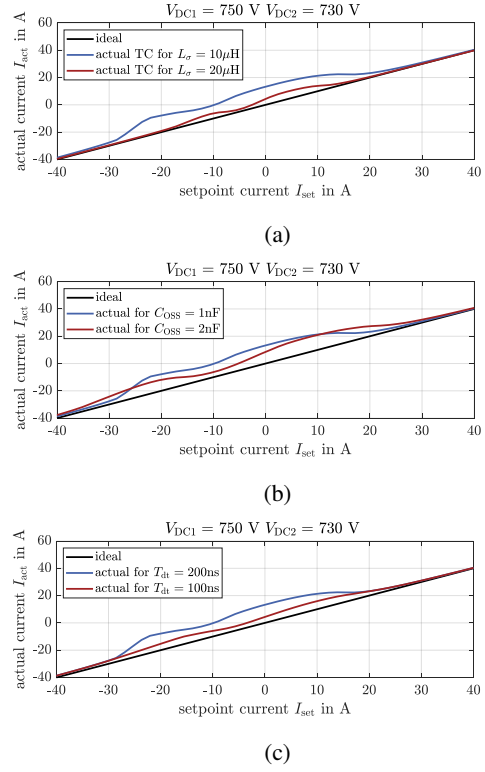

Fig. 7. Variation of system parameter and influence on the calculated transfer characteristic in buck operation (a) L_σ (b) C_{OSS} (c) T_{dt} (All parameter according to table I if not stated otherwise)

Each of these steps is designed in a modular fashion, enabling each functional group to be altered and tailored to specific optimization targets.

A. Data acquisition

During the data acquisition step, it is essential to measure the non-linear TC of the DAB for all relevant voltage sets, with a defined interpolation step, $S_{\text{VDC}} = [V_{\text{DC1}} \ V_{\text{DC2}}]$ of the system. The measurement system must possess the same system parameters as the compensated system. Interpolating the voltage set S_{VDC} is crucial to reduce computational effort for implementation later on. However, increasing the interpolation step may result in reduced method performance. Alternatively, measurement data can be substituted with simulation or calculation data if the model accuracy is sufficient.

B. Curve fitting

The invertible function must have the following properties in order to be used for the MFBL method:

- F_{fit} has to bijective to be invertible
- F_{fit} should have as few parameter as possible
- F_{fit} must be sufficiently accurate to handle both the big and small S-shaped function

In this paper, a modified sigmoid function is utilized for the curve fitting as shown in (6). This sigmoid function offers several advantages, being described with only four parameters $S_{\text{Sigmoid}} = [a \ b \ c \ d]$, while also being reasonably adjustable
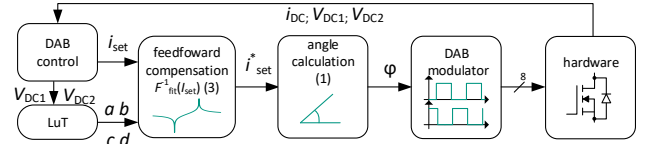

Fig. 8. Block diagram of the DAB system with feedforward compensation

to achieve both big S-shaped and small S-shaped contours. However, a notable disadvantage is that this function is not bijective over the entire operating range. As a result, the compensation interval using the modified sigmoid function is limited. The resulting inverted function $F_{\text{fit}}^{-1}(I_{\text{set}})$ is depicted in (7) with the respective interval depending on the parameter set S_{Sigmoid}.

$$F_{\text{fit}}(I_{\text{set}}) = \frac{1}{a + e^{-bI_{\text{set}}+c}} + d \approx I_{\text{act}} \qquad (6)$$

$$F_{\text{fit}}^{-1}(I_{\text{set}}) = \frac{c - \ln\left(\dfrac{1}{I_{\text{set}} - d} - a\right)}{b} = I_{\text{set}}^*$$

$$\text{with } d < I_{\text{set}} < d + \frac{1}{a} \qquad (7)$$

An example of the restricted fitting interval is illustrated in Fig. 10. The green marked area represents the feasible fitting interval defined by the invertibility of the Sigmoid function
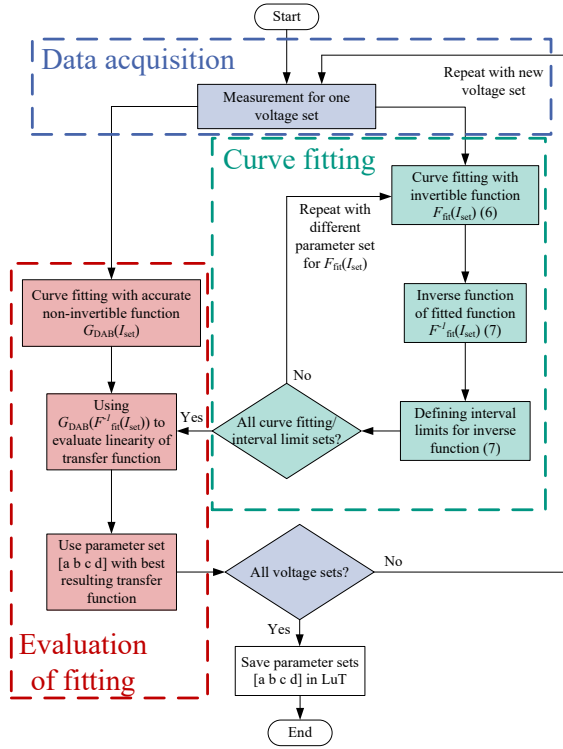
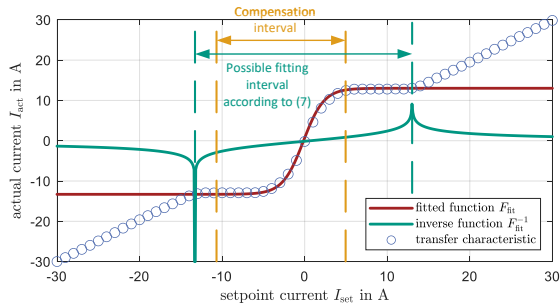Fig. 9. Flow chart of the measurement data driven function based linearization (MFBL) method

Fig. 10. Definition of intervals for the Sigmoid function

TABLE I
PARAMETER OF THE TESTBENCH

Symbol	Meaning	Value
	DAB parameter	
P	nominal output Power	40 kW
$V_{\mathrm{DC1/2}}$	In- Output voltage range	500 V-850 V
f_{sw}	Switching frequency	50 kHz
$C_{\mathrm{OSS,eq}}$	output capacitance @ 700 V	1 nF
T_{dt}	Inverter deadtime	200 ns
	Transformer parameter	
n	winding ratio	1 : 1
$L_{\sigma,\mathrm{T}}$	Leakage inductance	10 µH
$L_{\mathrm{h,T}}$	Magnetizing inductance	1 mH

a highly accurate fit $G^*_{\mathrm{DAB}}(I_{\mathrm{set}}) = I_{\mathrm{act}}$, which does not have the restrictions of being bijective and having the same function for all operation points like the invertible fitting function. All inverse functions are tested with this non-invertible function. The one that best fits $G^*_{\mathrm{DAB}}(F^{-1}_{\mathrm{fit}}(I_{\mathrm{set}})) = I_{\mathrm{act}} \approx I_{\mathrm{set}}$ is selected for each respective voltage set S_{VDC}. In this paper, a sum of six to eight sinusoidal terms is employed, resulting in a total of 18 to 24 parameters for each voltage set. The resulting function $G^*_{\mathrm{DAB}}(I_{\mathrm{set}})$ is presented in (8). Additionally, a secondary condition is defined as a performance metric. The gradient of the resulting transfer function $G_{\mathrm{DAB}}(I_{\mathrm{set}})$ must always be greater than zero to avoid controller instabilities.

$$G^*_{\mathrm{DAB}}(I_{\mathrm{set}}) = \sum_{i=1}^{N} p(i) \cdot \sin\left(k(i) \cdot I_{\mathrm{set}} + l(i)\right) = I_{\mathrm{act}}$$
$$\text{with } 6 \leq N \leq 8 \quad (8)$$

The resulting set S_{Sigmoid} with the best properties and the respective compensation interval will be stored in a Look up Table (LuT) and used by the controller of the DAB (cf. Fig. 8).
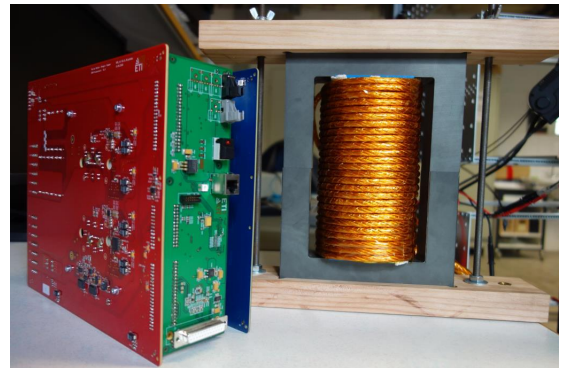
V. EXPERIMENTAL VALIDATION

Fig. 11. Hardware setup of the DAB

(6). Further reduction of the fitting interval is achievable, as the feedforward approach does not need to be utilized at all possible operation points. Consequently, this results in a compensation interval that can be symmetrical or asymmetrical and can be optimized based on the optimization criteria of the resulting compensation. An arbitrary example is depicted in Fig. 10 in yellow.

C. Evaluation of fitting

To optimize the feedforward function $F^{-1}_{\mathrm{fit}}(I_{\mathrm{set}})$ for the best linearity and lowest deviation from the ideal transfer characteristic, an offline model is essential. In this process, the data obtained during the data acquisition stage is utilized to obtain

To evaluate the performance of the MFBL, measurements are conducted on a 40kW DAB prototype, as depicted in Fig. 11. The relevant parameters of the system are listed in table I. Two performance indicators are defined to facilitate the quantification of the method's performance. The Maximum Error (ME) in (9) represents the maximum deviation from the ideal transfer characteristic, while the Mean Square Error (MSE) in (10) denotes the mean quadratic deviation from the ideal transfer characteristic.

$$\Delta I_{\text{act,max}} = \max\left[|I_{\text{act}} - I_{\text{set}}|\right] \tag{9}$$

$$\Delta I_{\text{act,MSE}} = \frac{1}{N} \sum_{n=-I_{\text{set,max}}}^{I_{\text{set,max}}} (I_{\text{act}}(n) - I_{\text{set}}(n))^2 \tag{10}$$

First the three fundamental transfer characteristics are presented in Fig. 12. Figure 12 (a) depicts a big S-shaped function in buck operation, Fig. 12 (b) displays a big S-Shape with boost operation and Fig. 12 (c) shows a small S-Shape occurring for unity operation. A significant improvement of the non-linear transfer characteristic for all three cases can be observed. Zooming in on the unity transfer characteristic steps can be seen in the compensated transfer characteristics. This is due to the finite resolution of the modulator and the necessary deviation in φ is too small to achieve with the given signal processing. The resolution is limited by the FPGA frequency of 150 MHz and therefore a minimal angular change in φ of $0.0021°$.

As mentioned previously, interpolation of the voltage steps is necessary. In this paper, an evenly distributed interpolation is employed due to its simplicity of implementation. To evaluate the performance of the MFBL with interpolated voltage sets S_{VDC}, different interpolation steps ranging from $V_{\text{step}} = 1$ V to $V_{\text{step}} = 6$ V are measured and compared to the non-compensated transfer characteristic. The Maximum Error (ME) for different interpolation steps is depicted in Fig. 13 (a). It is observed that for all interpolation steps, the compensated system exhibits a lower ME compared to the non-compensated one. Each interpolation step behaves similarly, with an increase in ME during the transition from a small S-Shape to a big S-Shape. Regarding the Mean Square Error (MSE) shown in Fig. 13 (b), a similar behavior is observed. The MSE is significantly reduced using the MFBL for all voltage sets S_{VDC}. For future work, a non-even distribution might be beneficial to further reduce the ME and MSE at these operation points. The controller performance using MFBL is shown in 14. It can be seen that the controller achieves the setpoint current significant faster with MFBL compared to the reference measurement. The reference measurement stays at around 12 A for more then $500 \ \mu$s until it reaches the setpoint current. This is due to the plateau visible in the transfer characteristic which needs a bigger change in φ then expected by the controller. This leads to small changes in φ caused by the I-controller which do not result in a change in the measured DC current. Only when the
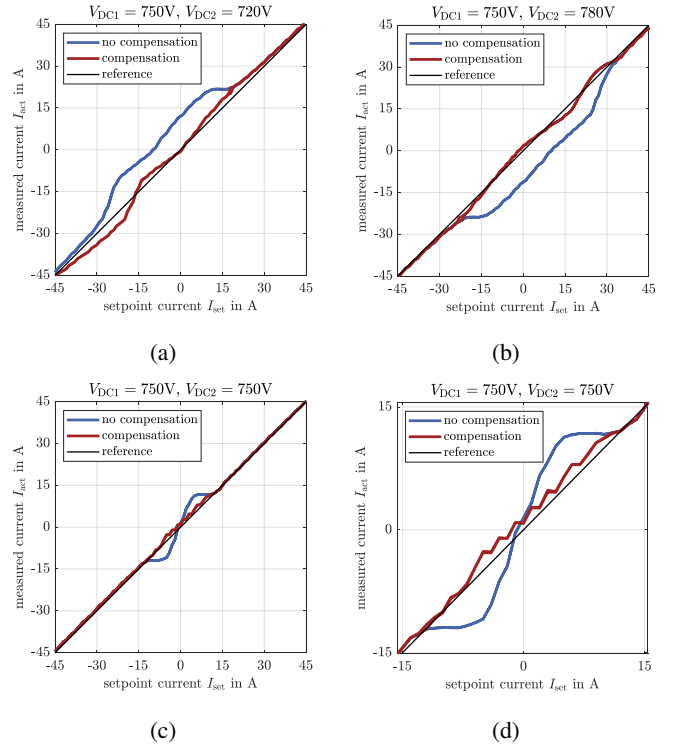

Fig. 12. Comparison of the measured TC with no compensation and with the MFBL method (a) buck operation (b) boost operation (c) unity operation (d) unity operation zoom in

plateau is overcome, the current does change to the desired value.

VI. CONCLUSION

This paper explores the influence of the Zero Voltage Switching (ZVS) transition on the transfer characteristic of the Dual Active Bridge (DAB). Various system parameters such as the stray inductance L_σ, the MOSFET output capacitance C_{OSS}, and the deadtime T_{dt} are analyzed. Based on this analysis, an easy-to-implement compensation method in the form of Measurement Data-Driven Function-Based Linearization (MFBL) is introduced. The algorithm for determining a compensation function $F^{-1}(I_{\text{set}})$ is outlined, and the requirements of such a function are elucidated. Measurement results obtained from a 40kW DAB prototype validate the impact of the ZVS transition and demonstrate a significant enhancement in the transfer characteristic using the MFBL method. Notably, even when interpolating, improvements are evident for all operation points of the DAB, encompassing both small S-Shaped and big S-Shaped transfer characteristics. The controller performance is significantly improved by reducing the time to reach the setpoint using the MFBL.
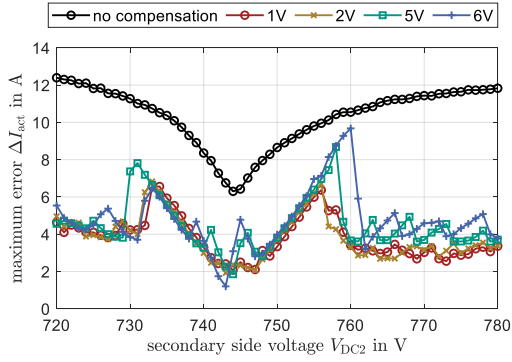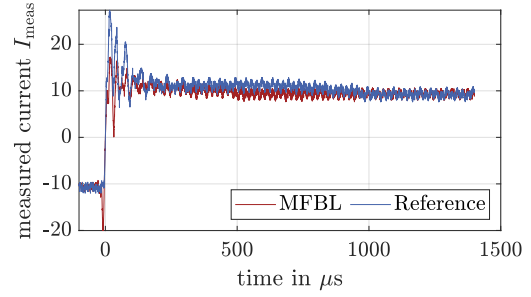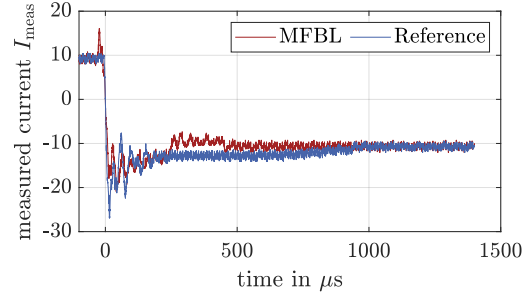
(a)
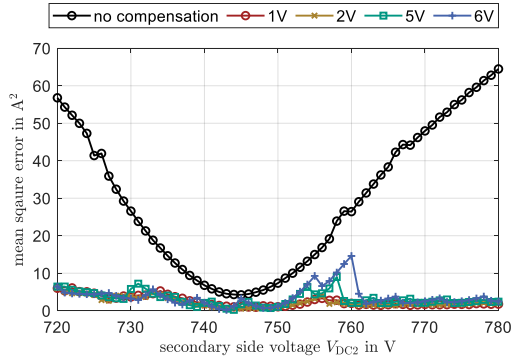
(b)

Fig. 13. Measured error compared to perfect linearity with different interpolation voltage steps (a) maximum error for different voltage transfer ratios at $V_{DC1} = 750V$ (b) mean square error for different voltage transfer ratio at $V_{DC1} = 750V$

(a)

(b)

Fig. 14. Measured setpoint change for $V_{DC1} = V_{DC2}$ from $I_{DC2} = 10A$ to $I_{DC2} = -10A$ and $I_{DC2} = -10A$ to $I_{DC2} = 10A$

REFERENCES

[1] R. W. A. A. De Doncker, D. M. Divan and M. H. Kheraluwala, "A three-phase soft-switched high-power-density DC/DC converter for high-power applications," in IEEE Transactions on Industry Applications, vol. 27, no. 1, pp. 63-73, Jan.-Feb. 1991

[2] M. Liserre, G. Buticchi, M. Andresen, G. De Carne, L. F. Costa and Z. -X. Zou, "The Smart Transformer: Impact on the Electric Grid and Technology Challenges," in IEEE Industrial Electronics Magazine, vol. 10, no. 2, pp. 46-58, June 2016

[3] P. Purgat, N. H. van der Blij, Z. Qin and P. Bauer, "Partially Rated Power Flow Control Converter Modeling for Low-Voltage DC Grids," in IEEE Journal of Emerging and Selected Topics in Power Electronics, vol. 8, no. 3, pp. 2430-2444, Sept. 2020

[4] L. Xue, Z. Shen, D. Boroyevich, P. Mattavelli and D. Diaz, "Dual Active Bridge-Based Battery Charger for Plug-in Hybrid Electric Vehicle With Charging Current Containing Low Frequency Ripple," in IEEE Transactions on Power Electronics, vol. 30, no. 12, pp. 7299-7307, Dec. 2015

[5] T. Merz, F. Sommer, R. Schwendemann, H. Sui, M. Hiller, "Error Storage Based Online Linearization of the Nonlinear Transfer Function of a High Power Dual Active Bridge," ICPE 2024-ECCE Asia - 10th International Power Electronics and Motion Control Conference, 2024.

[6] F. Sommer, N. Menger, T. Merz, N. Soltau, S. Idaka and M. Hiller, "Time Domain Modeling of Zero Voltage Switching behavior considering Parasitic Capacitances for a Dual Active Bridge," 2023 11th International Conference on Power Electronics and ECCE Asia (ICPE 2023 - ECCE Asia), Jeju Island, Korea, Republic of, 2023, pp. 13-20

[7] B. Zhao, Q. Song, W. Liu and Y. Sun, "Dead-Time Effect of the High-Frequency Isolated Bidirectional Full-Bridge DC–DC Converter: Comprehensive Theoretical Analysis and Experimental Verification," in IEEE Transactions on Power Electronics, vol. 29, no. 4, pp. 1667-1680, April 2014

[8] J. -i. Itoh, K. Kawauchi and H. Watanabe, "Non-linear Dead-time Error Compensation Method of Dual Active Bridge DC-DC Converter for Variable DC-bus Voltage," 2018 International Conference on Smart Grid (icSmartGrid), Nagasaki, Japan, 2018, pp. 208-213

[9] M. S. M. Jagau, T. N. Allgaeu, P. M. Patt, and T. N. Allgaeu, "Nonlinear Output Characteristics of DAB Converter caused by ZVS Transition," no. May, pp. 10–12, 2016.

[10] G. Zieglmaier, F. Sommer, T. Merz and M. Hiller, "Highly Dynamic Voltage Control of a Dual Active Bridge over the Full Voltage Range by Operating Point Dependent Manipulated Variable Limitation," PCIM Europe 2023; International Exhibition and Conference for Power Electronics, Intelligent Motion, Renewable Energy and Energy Management, Nuremberg, Germany, 2023, pp. 1-10, doi: 10.30420/566091325.

[11] F. Sommer, N. Menger, T. Merz, N. Soltau, S. Idaka and M. Hiller, "Design and Characterization of a 500 kW 20 kHz Dual Active Bridge using 1.2 kV SiC MOSFETs," 2022 International Power Electronics Conference (IPEC-Himeji 2022- ECCE Asia), Himeji, Japan, 2022, pp. 1390-1397, doi: 10.23919/IPEC-Himeji2022-ECCE53331.2022.9807023.